Available online at www.sciencedirect.com
SCIENCE DIRECT®
Journal of Solid State Chemistry 177 (2004) 231–244
JOURNAL OF SOLID STATE CHEMISTRY
http://elsevier.com/locate/jssc

Local crystal chemistry, induced strain and short range order in the cubic pyrochlore $(Bi_{1.5-\alpha}Zn_{0.5-\beta})(Zn_{0.5-\gamma}Nb_{1.5-\delta})O_{(7-1.5\alpha-\beta-\gamma-2.5\delta)}$ (BZN)

R.L. Withers,[a,*] T.R. Welberry,[a] A.-K. Larsson,[b] Y. Liu,[a] L. Norén,[a] H. Rundlöf,[c] and F.J. Brink[a,1]

[a] *Research School of Chemistry, Australian National University, GPO Box 4, Canberra ACT 0200, Australia*
[b] *Research School of Physical Sciences and Engineering, Australian National University, Canberra ACT 0200, Australia*
[c] *Neutronforskningslaboratoriet i Studsvik, Uppsala Universitet, S 611 82 Nyköping, Sweden*

Received 9 April 2003; received in revised form 16 July 2003; accepted 24 July 2003

Abstract

Clear evidence (in the form of structured diffuse scattering) is found for short range ordering of metal ions and associated induced structural relaxation in two members of the cubic BZN pyrochlore $(Bi_{1.5-\alpha}Zn_{0.5-\beta})(Zn_{0.5-\gamma}Nb_{1.5-\delta})O_{(7-1.5\alpha-\beta-\gamma-2.5\delta)}$ solid solution. An average neutron powder diffraction structure refinement is carried out for one of these. Electron probe micro-analysis suggests that the primary mechanism for non-stoichiometry in cubic BZN is the removal of ZnO from the nominally fully occupied $(Bi_{1.5}Zn_{0.5})(Zn_{0.5}Nb_{1.5})O_7$ end-member. A detailed bond valence sum analysis of a recently reported average crystal structure is used to suggest possible local cation ordering schemes along with the induced displacive relaxation that is likely to accompany such local cation ordering. The observed diffuse distribution is qualitatively interpreted via Monte Carlo modelling.

Keywords: Structured diffuse scattering; Local mutation ordering; Monte Carlo modelling

1. Introduction

There exist two structurally distinct, ternary phases in the Bi_2O_3–ZnO–Nb_2O_5 (BZN) system which exhibit high dielectric constants (ε), low dielectric losses and compositionally tunable temperature coefficients of capacitance (τ_c) [1–8]. Such materials make attractive candidates as resonators and decoupling capacitors in microwave circuits, particularly when linked with their relatively low sintering temperatures. Growing technological interest in these materials has recently led to the extensive investigation of their dielectric properties [1–8]. Structural investigations, however, have been rather more limited [9–10].

The two phases were initially reported to be of 'orthorhombically distorted', and conventional cubic, $A_2B_2O_6O'$ pyrochlore structure type respectively with nominal stoichiometries given by $Bi_2Zn_{2/3}Nb_{4/3}O_7$ and $(Bi_{1.5}Zn_{0.5})(Zn_{0.5}Nb_{1.5})O_7$, respectively. Wang et al. [3] reported that the phases were actually solid solutions with stoichiometries given by the formula $(Bi_{3x}Zn_{2-3x})(Zn_xNb_{2-x})O_7$ and composition ranges $0 \leqslant \frac{1}{2}(2-3x) \leqslant 0.04$ for the former 'orthorhombic pyrochlore' phase and $0.18 \leqslant \frac{1}{2}(2-3x) \leqslant 0.25$ for the latter conventional cubic pyrochlore phase. Subsequently, Levin et al. have shown that the former phase is actually of zirconolite, rather than pyrochlore, structure type [9] but confirmed that the second cubic BZN phase is indeed of average pyrochlore structure type, albeit with stoichiometry $(Bi_{1.5}Zn_{\sim 0.42})(Zn_{0.5}Nb_{1.5})O_{\sim 6.92}$ and with extensive displacive disorder on both the A and O′ sites [10].

The extensive displacive disorder of the latter cubic BZN phase has been associated with anomalous low temperature glass-like dielectric behavior [8] but does not occur for the zirconolite type phase. The structural origin of this behavior is far from clear. From the crystal chemical point of view (see below), extensive displacive

*Corresponding author. Fax: +612-612-50750.
E-mail address: withers@rsc.anu.edu.au (R.L. Withers).
[1] Also at the Electron Microscope Unit, Research School of Biological Sciences, Australian National University, Canberra ACT 0200, Australia.

0022-4596/$ - see front matter © 2003 Elsevier Inc. All rights reserved.
doi:10.1016/j.jssc.2003.07.005

Table 1
Refinement results obtained for the various models described in the text

	Atom	Occupancy	Wyckoff position	x	y	z	$U_{iso}(Å^2) \times 100$
Model 1	Bi(A)/Zn(A)	0.75/0.1525	16d (−3m)	0.5	0.5	0.5	8.4(4)
M1, (*10*)		0.75/0.21	*16d (−3m)*	0.5	0.5	0.5	9.87(11)
Model 2		0.75/0.162	96g (··m)	0.468(1)	0.515(1)	0.515(1)	1.6(2)
M2, (*10*)		0.75/0.21	*96g (··m)*	0.46731(34)	0.51499(35)	0.51499(35)	1.62(5)
Model 3		**0.75/0.163**	**96h (··2)**	**0.5**	**0.4732(2)**	**0.5268(2)**	**1.7(2)**
	Nb(B)/Zn(B)	0.75/0.25	16c (−3m)	0	0	0	1.3(1)
		0.75/0.25	*16c (−3m)*	0	0	0	1.79(3)
		0.75/0.24	*16c (·−3m)*	0	0	0	1.28(7)
		0.75/0.25	16c (·−3m)	0	0	0	1.37(2)
		0.75/0.24	**16c (·−3m)**	**0**	**0**	**0**	**1.29(8)**
	O	1	48f (2·mm)	0.3196(4)	1/8	1/8	2.5(1)
		1		0.3196(1)	1/8	1/8	2.34
		0.972	48f (2·mm)	0.3194(1)	1/8	1/8	2.03(6)
		1		0.31984(7)	1/8	1/8	2.28
		0.974	**48f (2·mm)**	**0.3194(2)**	**1/8**	**1/8**	**2.05(5)**
	O′	0.92	8b (−43m)	3/8	3/8	3/8	7.0(7)
		0.92		3/8	3/8	3/8	11.28(21)
		0.972	96g (..m)	0.349(3)	0.349(3)	0.379(4)	4.6(15)
		0.92		0.34403(27)	0.34403(27)	0.3776(5)	2.05(21)
		0.961	**32e (.3m)**	**0.3937(15)**	**0.3937(15)**	**0.3937(15)**	**5.7(6)**

disorder is perhaps not unexpected given the necessary presence of the rather small Zn^{2+} ion [11] on the (6 + 2)-fold coordinated pyrochlore A site and the difference in valence of the cations occupying the pyrochlore B site. The known limits of structural stability for the ideal cubic pyrochlore structure type [10,12] suggest that it should not be possible for Zn^{2+} to occupy the A site without significant local structural distortion.

One could therefore anticipate significant strain on the local scale perhaps leading to short range order and structured diffuse scattering. Levin et al. [10] also anticipated the likelihood of local ordering and associated structural relaxation but were unable to find any direct diffraction evidence for such short range order. The primary purpose of the current paper is to report clear evidence for short range order (in the form of structured diffuse scattering detected via a careful electron diffraction study) and its qualitative interpretation via Monte Carlo modelling.

2. Crystal chemical considerations

We begin with a bond valence sum analysis of the recently reported (see Ref. [10]) $Fd\bar{3}m$ average cubic pyrochlore structure of $(Bi_{1.5}Zn_{0.42})(Zn_{0.5}Nb_{1.5})O_6O'_{0.92}$ ($a = 10.5616$ Å; A on 16d at $\frac{1}{2},\frac{1}{2},\frac{1}{2}$; B on 16c at 000; O on 48f at $x,\frac{1}{8},\frac{1}{8}$ with $x = 0.3196$ and O′ on 8b at $\frac{3}{8},\frac{3}{8},\frac{3}{8}$) using the bond valence parameters (R_0's) of Brese and O'Keeffe [13]. For the purposes of the following bond valence sum analysis, we ignore the 4% vacancy concentration reported for the A site and the 8% vacancy concentration reported for the O′ site in Table 1 of Levin et al. [10]) i.e., we effectively assume $(Bi_{1.5}Zn_{0.5})(Zn_{0.5}Nb_{1.5})O_6O'_1$ stoichiometry.

There are various possible ways of describing the ideal cubic pyrochlore structure type. One such description is in terms of intergrown $O'A_2$ and $\square B_2$ ($\square$ a vacancy) anti-cristobalite tetrahedral framework sub-structures (see Fig. 1a) linked together by OA_2B_2 tetrahedra i.e., a 'defect fluorite' type description (see e.g., Ref. [12]). For the purposes of this discussion, however, we will use an alternative commonly used description involving two intergrown component sub-structures—a B_2O_6 octahedral corner-connected sub-structure (see Fig. 1b) and an $O'A_2$ tetrahedral corner-connected sub-structure of anti-cristobalite structure type (see Fig. 1c). These two component sub-structures are by no means independent of one another, the A cations of the latter, for example, are bonded reasonably strongly to the O ions of the former. Breaking the ideal cubic pyrochlore structure up in this way is nonetheless a valid and quite useful means of investigating the crystal chemistry of the overall structure.

2.1. The B_2O_6 octahedral sub-structure

Consider firstly the former B_2O_6 octahedral corner-connected sub-structure (see Fig. 1b). The B cation in this sub-structure is octahedrally coordinated by 6 O ions at an average distance $R(B-O) = \sqrt{\{(x-1/4)^2 + 2(1/8)^2\}} \times 10.5616$ Å which is dependent on the one unknown fractional coordinate of the ideal pyrochlore structure type, the x coordinate of the O ion, and the cubic lattice parameter a, in Levin et al.'s case = 10.5616 Å [10].

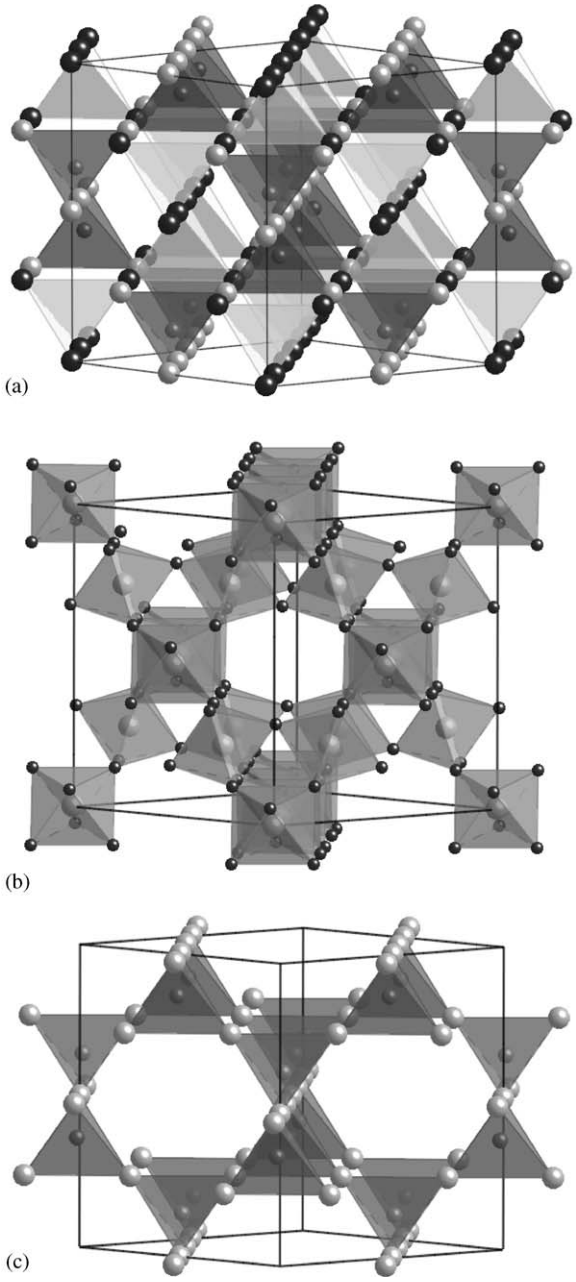

Fig. 1. Two possible ways of describing the ideal cubic pyrochlore structure type. (a) Intergrown $O'A_2$ (the darker tetrahedra represent $O'A_4$ tetrahedra) and $\square B_2$ (the lighter tetrahedra represent $\square B_4$ tetrahedra, $\square$ a vacancy) anti-cristobalite tetrahedral framework sub-structures linked together by OA_2B_2 tetrahedra (not shown). (b) and (c) two constituent network sub-structures that together comprise the ideal pyrochlore structure type. The first (b) is a B_2O_6 array of corner-connected, cation-centered BO_6 octahedra while the second (c) is an $O'A_2$ array of corner-connected, oxygen-centered tetrahedra (of ideal anti-β-cristobalite structure type, cf. with a).

For Nb^{5+} in the B site, the ideal $B-O$ distance $R(Nb-O)$ is given by that distance which corresponds to an apparent valence (AV) (see Ref. [13]) of $\frac{5}{6}$. From Ref. [13], this distance is given by $1.911-0.37\ln(\frac{5}{6}) = 1.9785$ Å. For Zn^{2+} in the same B site, the equivalent ideal B–O distance $R(Zn-O) = 1.704-0.37\ln(\frac{2}{6}) = 2.1105$ Å again using the R_0 parameters listed in [13]. Note that these two ideal bond lengths are not too far apart. Thus while relaxations of the O array associated with the local distribution of Nb^{5+} and Zn^{2+} on the B sites should be expected, the magnitude of these local relaxations should not be that large, despite the big difference in valence between these two cations. This is reflected in the relatively small displacement parameters refined for the B and O sites of the average structure (see Ref. [10] and Table 1 below).

Table 2
Bond valence sums (AV's) for the cubic pyrochlore average structure

A	B	AV(A)	AV(B)	AV(O)	AV(O′)
Bi	Nb	2.461	4.635	1.969	2.377
Bi	Zn	2.461	2.649	1.307	2.377
Zn	Nb	0.858	4.635	1.693	0.828
Zn	Zn	0.858	2.649	1.031	0.828

Given that the average occupancy of the B site is close to $\frac{3}{4}Nb+\frac{1}{4}Zn$, the expected average $B-O$ bond length, $R(B-O)$ should be such that $AV(B) = 6\times\frac{1}{4}\times\exp\{(1.704-R)/0.37\}+6\times\frac{3}{4}\times\exp\{(1.911-R)/0.37\} = \frac{1}{4}\times 2+\frac{3}{4}\times 5 = 4.25$. This occurs for $R = 1.9967$ Å which is very close to the refined value of 2.0065 Å [10]. An average $R(B-O)$ bond length of 1.9967 Å occurs for $x = 0.3170$ given the relation between $R(B-O) = \sqrt{\{(x-\frac{1}{4})^2+2(\frac{1}{8})^2\}}\times 10.5616$ Å and x. The bond valence sum prediction for the value of x is thus 0.3170. Experimentally, Levin et al. [10] refined x to be 0.3196 for their sample. The final refined value of x for our sample 2 (see below) is very similar at 0.3194 (see Table 1). The bond valence sum predicted and refined values are thus remarkably close. The 'average' B cation is thus happily bonded in the average pyrochlore structure.

Locally, however, whenever Nb^{5+} is in the B site, it needs to suck in the 6 surrounding O ions slightly from the average distance of ~2.01 Å to the ideal value of ~1.98 Å whereas, when Zn^{2+} is in the B site, it needs to repel the 6 surrounding O ions from ~2.01 to ~2.11 Å (accordingly, bond valence sum calculations using the refined average structure fractional co-ordinates (see Table 2) show Nb^{5+} somewhat under-bonded and Zn^{2+} significantly more over-bonded in the B site). From the point of view of strain minimization, the most efficient means of achieving this would be for the stoichiometry of each of the two $\square B_4$ tetrahedra surrounding each Zn^{2+} ion in a B site (see Figs. 1a and b) to have the average stoichiometry i.e., $\square Nb_3Zn$ so that the 6 O ions surrounding the central Zn^{2+} ion in the B site can be simultaneously repelled from the Zn^{2+} site and, as it were, absorbed by the neighboring Nb^{5+} ions (see Fig. 1b).

2.2. The $O'A_2$ anti-cristobalite tetrahedral sub-structure

Now consider the second $O'A_2$ tetrahedral corner-connected sub-structure of anti-cristobalite structure type (see Fig. 1c). The O′ anion in this sub-structure is tetrahedrally coordinated by 4 A cations at a distance $R(O'-A) = (\sqrt{3}/8)a = 2.287$ Å determined solely by the cubic lattice parameter a. For Bi^{3+} in the A site, the ideal $O'-A$ distance $R(O'-Bi)$ is given by that distance which corresponds to an AV of $\frac{2}{4}$. From [13], this distance is given by $2.094-0.37\ln\frac{2}{4} = 2.3505$ Å whereas for Zn^{2+} in the A site, this ideal $O'-A$ distance $R(O'-Zn) = 1.704 - 0.37\ln\frac{2}{4} = 1.9605$ Å. Note that this time these two ideal bond lengths differ quite significantly from each other and from the average $O'-A$ distance of 2.287 Å.

Thus considerable strain relaxation of the $O'A_2$ array can be expected associated with the local distribution of Bi^{3+} and Zn^{2+} on the A sites with the O′, Bi^{3+} and Zn^{2+} ions moving in such a way as to expand the local O'–Bi^{3+} distances (from 2.287 to ~2.351 Å) and significantly contract the O'–Zn^{2+} distances (from 2.287 to ~1.961 Å) within each local $O'A_4$ tetrahedra. This is again reflected in the much larger thermal parameters refined for the A and O′ sites of the average structure (see Ref. [10] and Table 1 below).

From the point of view of strain minimization, the most efficient means of achieving this would be for the stoichiometry of both of the $O'A_4$ tetrahedra surrounding each Zn^{2+} ion in an A site (see Fig. 1c) to have the average stoichiometry i.e., $O'Bi_3Zn$ so that the 2 O′ ions on either side of the central Zn^{2+} ion can simultaneously contract in towards it along the local ⟨111⟩ direction (thereby significantly alleviating its chronic under-bonding in the average structure, see Table 2) and away from the neighboring Bi^{3+} ions (see Fig. 1c). Given that the occupancy of the A site is ~$\frac{3}{4}$Bi+$\frac{1}{4}$Zn, the expected average $O'-A$ bond length, $R(O'-A)$ should be such that $AV(O') = 4\times\frac{1}{4}\times\exp\{(1.704-R)/0.37\} + 4\times\frac{3}{4}\times\exp\{(2.094-R)/0.37\} = 2$. This occurs for $R = 2.2847$ Å which is indeed quite close to $(\sqrt{3}/8)a = 2.287$ Å.Thus the O′ ion will again be relatively happily bonded, but only when surrounded by 3 Bi's and 1 Zn (see Table 3).

2.3. Inter-substructure interactions

By breaking the ideal pyrochlore structure up into B_2O_6 and $O'A_2$ sub-structures attention has to date focussed on satisfying the bond valence sum requirements of the B and O′ ions. What about the remaining A and O ions? The A cation is in an essentially hexagonal prismatic site surrounded by 6 equatorial O ions and 2 apical O′ ions. Bond valence sum calculations make it clear that the A cation in this site is always significantly under-bonded, particularly when Zn^{2+} occupies the site (see Table 2). The local distortion of each $O'Bi_3Zn$ tetrahedron described above, in particular the significant shortening of O′–Zn–O′ linkages along local ⟨111⟩ directions will, however, go a long way towards remedying this underbonding of the Zn^{2+} ions in the A site. A simultaneous reduction in the two apical Zn–O′ distances from 2.287 to 1.9605 Å, for example, leads to an increase in the AV of the central Zn ion of ~0.6 valence units [13].

In the case of Bi^{3+} ions in the A site, however, given that the 2 surrounding apical O′ ions are already reasonably happily bonded (if not slightly over-bonded) in the average structure, it is clear that the under-bonded Bi^{3+} cation cannot improve the situation by moving closer to these ions but must instead move off-center towards one or other of the 6 surrounding equatorial O ions. This is again clearly reflected in the refined displacement parameters of the A cation site in the average structure (see Ref. [10] and Table 1 below).

For the Bi cations to significantly improve their under-bonding in this manner, however, requires moving towards an O ion that is already also under-bonded. The O ion occupies an off-center position in an A_2B_2 tetrahedral site. Its bond valence sum, or AV [13], depends upon the surrounding distribution of A and B cations. Assuming, as far as possible, Bi_3Zn stoichiometry for each A_4 tetrahedron and Nb_3Zn stoichiometry for each B_4 tetrahedron, limits the potential local A_2B_2 stoichiometry to one of 4 possibilities. The calculated AV of the O ion for each of these 4 possibilities is given in Table 4. Note that the O ion will be happily bonded when surrounded by 2 Bi's and 2 Nb's and thus cannot accept an incoming A cation. Otherwise it can expect to be under-bonded, particularly if Zn^{2+} occupies one of the B sites. In this situation, the local O ion would be happy to accept an incoming A cation. The question is: can all these local crystal requirements be simultaneously satisfied and, if so, how?

Table 3
AV's for O′ dependent upon local $[A_4]$ stoichiometry

	$[Bi_4]$	$[Bi_3Zn]$	$[Bi_2Zn_2]$	$[BiZn_3]$	$[Zn_4]$
$AV(O')[A_4]$	2.377	1.990	1.603	1.215	0.828

Table 4
AV's for O dependent upon local $[A_2B_2]$ stoichiometry

	$[Bi_2Nb_2]$	$[Bi_2NbZn]$	$[BiZnNb_2]$	$[BiZnNbZn]$
$AV(O)[A_2B_2]$	1.969	1.638	1.831	1.500

3. Experimental

3.1. Synthesis

The cubic BZN $(\frac{3}{2}-\alpha)BiO_{1.5}(1-[\beta+\gamma])ZnO(\frac{3}{2}-\delta)NbO_{2.5} \equiv (Bi_{1.5-\alpha}Zn_{0.5-\beta})(Zn_{0.5-\gamma}Nb_{1.5-\delta})O_{(7-1.5\alpha-\beta-\gamma-2.5\delta)}$ samples used in this study came from two different sources. The first, sample 1, was provided courtesy of Dr. H.L. Du and Prof. X. Yao of Xi'an Jiaotong University, China while the second, sample 2, was prepared in-house. Both were synthesized by solid state reaction. The final sintering temperature for sample 1 was 940°C for 2 h after pre-heating at 800°C for 2 h.

The starting materials for the in-house synthesis, bismuth oxide (Bi_2O_3, 3 N, Koch–Light), zinc oxide (ZnO, 4N, Halewood) and niobium pentoxide (Nb_2O_5, 5 N, Atomergic), were initially dried at 130°C for 15 h. The nominal stoichiometric mixture was then ground in an agate mortar in ethanol for 30 min. A pre-reaction was performed by heating at 600°C for 2 h in a covered alumina crucible followed by a further 4 h heating at 800°C. The resultant powder was then re-ground, pressed into a pellet and sintered at 1150°C for a further 2 h. The resultant sintered pellet was then crushed into a powder for structural investigation. This 1150°C specimen (sample 2) was used for the neutron diffraction investigation. Both samples were investigated by electron diffraction and XRD.

3.2. Characterization

XRD data was collected using a Guinier-Hägg camera and Cu$K\alpha_1$ radiation. Si (NBS #640c, $a = 5.431195(9)$ Å at 22.5°C) was used as an internal standard in order to accurately determine unit cell parameters. Samples suitable for transmission electron microscope (TEM) work were prepared by the dispersion of finely ground material onto a holey carbon film. Electron diffraction patterns (EDPs) were obtained with a Philips EM 430 TEM.

Electron probe microanalysis (EPMA) was used to determine composition. Samples were prepared by pressing the powder into pellets followed by the application of a thin (~20 nm) carbon coat. The analyses were carried out at 15 kV and 2 nA using a JEOL 6400 scanning electron microscope (SEM) equipped with an Oxford Instruments light element EDS detector and Link ISIS SEMquant software. In order to minimize the atomic number, absorption, and fluorescence (ZAF) corrections [14], $Bi_2Zn_{2/3}Nb_{4/3}O_7$ was synthesized and used as a calibration standard.

3.3. Neutron diffraction

The neutron powder diffraction data were collected at the *R*2 research reactor at "Neutronforskningslaboratoriet" (NFL) in Studsvik, Sweden using the NPD powder diffractometer. Diffractograms were recorded at both 295 and 10 K using the in-house built detection system consisting of 35 ^{3}He detectors measuring the data in 2θ steps of 0.08° [15]. The sample was placed in a vanadium cylinder and the absorption factor was experimentally determined at $2\theta = 0°$ ($\mu R = 0.095$). The neutron flux is approximately $10^6\,cm^{-2}\,s^{-1}$ for the Cu (220)-monochromatization used, with a wavelength of approximately 1.471 Å.

A more accurate value of the neutron wavelength was derived by using the unit cell dimensions obtained from the X-ray diffraction data (see below) as "standard" and manually changing the neutron wavelength until the neutron refinement gave the same value to within a standard deviation. This obtained value for the neutron wavelength was 1.4707(4) Å. Data was collected between 4° and 139.92° in 2θ but the last 1.92° were treated as an excluded region in order to minimize the risk of intensities from reflections outside the detection range affecting the refined model.

4. Results and discussion

4.1. XRD

The cubic BZN cell parameter of sample 1 was refined to 10.5465(9) Å while that of sample 2 was refined to 10.5633(9)Å very close to the 10.5616(1)Å cell dimension reported by Levin et al. [10]. The variability of the cubic BZN cell dimension between the two samples while small nonetheless suggests that the cubic BZN phase may indeed be a solid solution, as suggested by Wang et al. [3].

4.2. Electron probe microanalysis

Electron probe microanalysis of the two samples was thus used to determine their composition. In order to minimize the atomic number, absorption, and fluorescence (ZAF) corrections [14], the zirconolite type phase of stoichiometry $Bi_2Zn_{2/3}Nb_{4/3}O_7$ was synthesized and used as a calibration standard.

The composition of sample 1 was found to be $Bi_{1.508(9)}Zn_{0.963(22)}Nb_{1.494(7)}O_{6.96}$ (assuming 6.96 oxygen atoms) while that of sample 2 was found to be $Bi_{1.499(11)}Zn_{0.805(29)}Nb_{1.500(8)}O_{6.805}$ (assuming 6.805 oxygen atoms) and $Bi_{1.542(11)}Zn_{0.828(30)}Nb_{1.543(8)}O_7$ (when recalculated to 7 oxygen atoms). The final results are based on the average of 12 analyses on each sample, the quoted errors were estimated from the standard deviation of the repeated measurements. As suggested by the above XRD results and in partial agreement with Wang et al. [3], it appears that the cubic BZN phase is indeed a narrow solid solution. In disagreement with the

stoichiometric formula suggested by Wang et al. [3] but in good agreement with the compositional analysis of Levin et al. [10], it would appear that the primary mechanism for non-stoichiometry is the removal of ZnO from the nominally fully occupied $Bi_{1.5}Zn_{1.0}Nb_{1.5}O_7$ ideal cubic BZN stoichiometry e.g., $Bi_{1.499(11)}Zn_{0.805(29)}Nb_{1.500(8)}O_{6.805}$ implies $\alpha = 0.001$, $\beta + \gamma = 0.195$, $\delta = 0.000$ in the formula $(\frac{3}{2} - \alpha)BiO_{1.5} \cdot (1 - [\beta + \gamma])ZnO \cdot (\frac{3}{2} - \delta)NbO_{2.5}$.

4.3. Neutron diffraction

The conclusion of the electron diffraction component of the recently reported detailed study of the cubic BZN $(Bi_{1.5}Zn_{0.42})(Zn_{0.5}Nb_{1.5})O_{6.92}$ composition [10] was that no extra scattering in addition to the Bragg reflections was present. However, in this study (see below) we detected very pronounced localized diffuse scattering of electrons for both samples 1 and 2. To make sure that our samples and that of Levin et al. [10] were closely related, neutron powder diffraction data from sample 2 was collected and the details of its average crystal structure re-refined.

In all the refinements described below, the overall stoichiometry was held at the above EPMA determined composition $Bi_{1.499(11)}Zn_{0.805(29)}Nb_{1.500(8)}O_{6.805}$. In the initial refinements, following Levin et al. [10], the Zn deficiency was presumed to be accommodated solely on the A site and the oxygen deficiency on the O′ site. This gives rise to an occupancy for Bi of 0.75 and for Zn of 0.1525 on the A site, an occupancy for Nb of 0.75 and for Zn of 0.25 on the B site, an occupancy for oxygen of 1 on the O site and 0.805 on the O′ site. In addition, the atomic displacement parameter (ADP) of the Bi and Zn ions on the A site as well as those of the Nb and Zn ions on the B site were constrained to be equal.

The refinement of the $Fd\bar{3}m$ average structure using isotropic ADP's (Model 1 in Table 1) converged quickly ($R_{wp} = 6.74\%$, $R_{w,all} = 5.72\%$ and $\chi^2 = 4.25$ with 6 structural and 20 profile parameters refined). The one unknown parameter of the ideal pyrochlore structure type, the x fractional co-ordinate of the O ion, refined to the value 0.3196, identical to the value reported by Levin et al. [10]. Similarly, the refined isotropic ADP's, while not identical, were again very similar to those reported by Levin et al. [10] for their sample. In particular, the refined displacement parameters associated with the $O'A_2$ sub-structure (those of the A and O′ ions) were an order of magnitude larger than those associated with the B_2O_6 sub-structure (the B and O ions). Likewise the refined isotropic displacement parameter of the O ion, while substantially smaller than those of the A and O′ ions, was again somewhat higher than normally accepted. For comparison purposes, the refined parameters obtained by Levin et al. [10] for the equivalent refinement are given in the second row of Table 1.

In order to carry out a more detailed comparison between the atomic displacement parameters in our sample 2 and those of Levin et al. [10], the structure was then re-refined using the same split atom model as [10] in which the A ion (Bi/Zn) was allowed to move away from the 16d (site symmetry $\bar{3}m$) $\frac{1}{2},\frac{1}{2},\frac{1}{2}$ position to the 96g (site symmetry m) x, y, y position, the O′ ion was likewise allowed to move away from the 8b (site symmetry $\bar{4}3m$) $\frac{3}{8},\frac{3}{8},\frac{3}{8}$ position to the 96g (site symmetry m) x, x, y position and the O ion was allowed anisotropic ADP's. The final, significantly improved residual R-values for this model were $R_{wp} = 4.76\%$, $R_{w,all} = 2.90\%$ and $\chi^2 = 2.12$ with 12 structural and 20 profile parameters refined. The refined parameters were again quite similar to those obtained by Levin et al. [10].

At this stage, the assumption that the oxygen deficiency is accommodated solely on the O′ site and the Zn deficiency on the A site was tested by refining the relative oxygen occupancy on the O and O′ sites as well as the relative occupancy of the Zn ion on the A and B sites subject to the constraint that the overall $Bi_{1.499(11)}Zn_{0.805(29)}Nb_{1.500(8)}O_{6.805}$ stoichiometry was maintained. The relative oxygen occupancies were refined first and a quite significant improvement in refinement statistics (to $R_{wp} = 4.37\%$, $R_{w,all} = 1.92\%$ and $\chi^2 = 1.79$) was obtained with the addition of only this one extra parameter. The oxygen occupancies of both the O and O′ sites refined to 0.972 i.e., there was no indication that the oxygen vacancies were preferentially located on either the O or O′ sites. The Zn occupancies were then refined but changed very little as did the refinement statistics (to $R_{wp} = 4.36\%$, $R_{w,all} = 1.88\%$ and $\chi^2 = 1.78$) i.e., the Zn vacancies are again overwhelmingly located on the A site. The Zn occupancies on the A and B sites refined to 0.162 (up from the initial 0.1525) and 0.24 (down from the initial 0.25). The final refined parameters for this model, Model 2, are given in the third row of Table 1. For comparison purposes, the equivalent Levin et al. refined parameters [10] are given in the fourth row of Table 1.

In this Model 2, the A ions are displaced by $0.015[\bar{2}11] \sim 0.39$ Å in the {111} plane perpendicular to the local O′–A–O′ ⟨111⟩ direction. Difference density plots of the earlier isotropic refinement show clearly that there is nothing special about this $[\bar{2}11]$ displacement direction in the {111} plane. Rather, the A ions should be thought of as being constrained to a donut of ~0.39 Å radius in the local {111} plane. This was shown by allowing the A ions to displace in the orthogonal $[0\bar{1}1]$ direction, again however perpendicular to the local O′–A–O′ ⟨111⟩ direction. Essentially equivalent refinement statistics were then obtained. The refined magnitude of the displacement this time was $0.0268[0\bar{1}1] = 0.40$ Å, but with a reduction of one positional parameter. This displacement direction was thus retained in the following refinements.

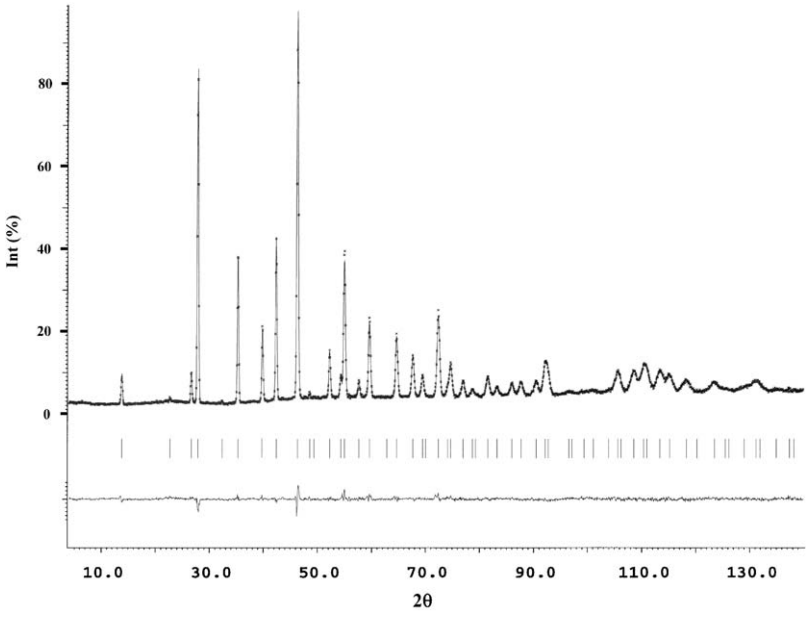

Fig. 2. The experimental neutron powder diffraction pattern of sample 2 along with the final (Model 3) refinement and difference plots.

The O′ ions for Model 2 likewise appear to be displaced ~ 0.026 [110] ~ 0.39 Å but this time in a local $\langle 110 \rangle$ direction. From the refinement point of view, this split atom model appears to describe the average structure very well albeit with relatively large isotropic displacement parameters (see row 3 of Table 1). However, while the ~ 0.40 Å anisotropic displacements of the more heavily scattering A ions in the {111} planes perpendicular to the local O′–A–O′ axes are clearly quite reliable and provide a reasonably strong constraint upon modelling of the local short range order, the apparent local displacement of the O′ ions along $\langle 110 \rangle$ directions is not so well-defined. The large ~ 0.39 Å average displacement of this ion as well as the $\langle 110 \rangle$ direction of the displacement give a fairly 'round' average positional distribution for these O′ ions. Similar average distributions may well also be describable by other displacements.

Some further models were therefore tested in a search for reliable indications of directional displacement restrictions on the O′ ions that could be used in the modelling of short range ordering. Our general conclusion, however, was that we could find no strong evidence from these average structure refinements for any specific direction of displacement of the O′ ion. The O′ portion of the structure could be equally well described by any of these models with a generally largish isotropic displacement parameter. Our final model (Model 3, bold in Table 4) restricted a shift of O′ to the $\langle 111 \rangle$ direction (Wyckoff position 32 ($3m$)) for crystal chemical reasons (see above and below) thereby reducing the number of positional parameters by one. The final refinement statistics were $R_{wp} = 4.36\%$, $R_{w,all} = 1.86\%$ and $\chi^2 = 1.78$. Fig. 2 shows the experimental diffraction pattern with the usual refinement and difference plots.

4.4. Electron diffraction

Electron diffraction is ideally suited to the detection of weak features of reciprocal space such as structured diffuse scattering as a result of the strong interaction of electrons with matter [16–18]. The EDPs shown below (see Fig. 3) were obtained from a crushed specimen of sample 1 as micro-analysis showed this to be the closest to the nominal ideal stoichiometry. Very similar EDPs, however, were also obtained from sample 2 (cf. for example the $\sim \langle 551 \rangle$ zone axis EDP of sample 2 shown in Fig. 4 with the equivalent EDP of sample 1 shown in Fig. 3a). In agreement with Levin et al. [10], no diffuse scattering was observed at either the exact $\langle 100 \rangle$ or $\langle 110 \rangle$ zone axis orientations. On tilting slightly away from these exact zone axis orientations, however, a characteristic, highly structured and quite reproducible diffuse intensity distribution was always observed. Fig. 3b, for example, shows a close $\langle 100 \rangle$ zone axis EDP obtained by tilting only a few degrees away from the exact $\langle 100 \rangle$ zone axis orientation while Fig. 3d shows a likewise close to $\langle 110 \rangle$ zone axis orientation obtained by also tilting only a few degrees away from the exact $\langle 110 \rangle$ zone axis orientation. Note the presence in both EDPs of strong blobs of diffuse intensity ("satellite reflections") at the $\mathbf{G} \pm \sim \langle 001 \rangle^*$ positions of reciprocal space (particularly apparent in Fig. 3d) along with the presence of diffuse streaking running through and connecting these diffuse blobs of

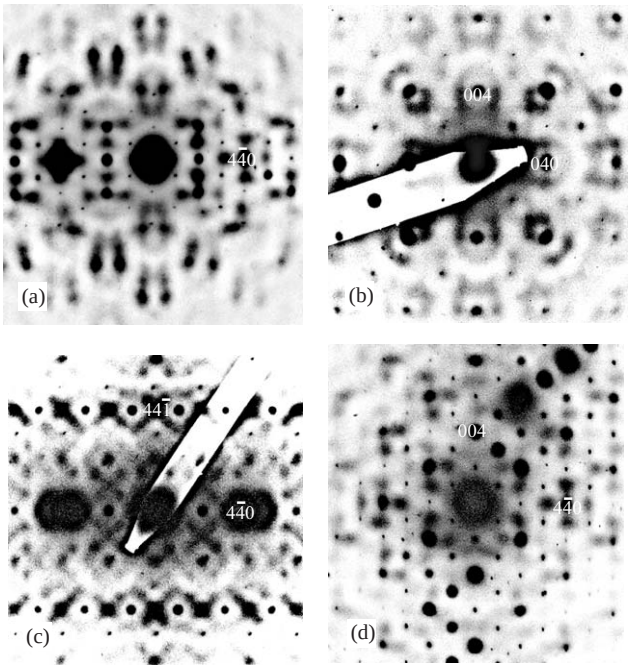

Fig. 3. Typical EDPs obtained from sample 1. (a) $\sim\langle 551\rangle$ zone axis EDP obtained by tilting $\sim 9^\circ$ away from the exact $\langle 110\rangle$ zone axis orientation keeping the $\langle 220\rangle^*$ systematic row excited. (b) A close to $\langle 001\rangle$ zone axis EDP obtained by tilting only a few degrees away from the exact $\langle 001\rangle$ zone axis orientation. (c) $\langle 118\rangle$ zone axis EDP obtained by tilting $\sim 10^\circ$ away from the $\langle 001\rangle$ orientation keeping the $\langle 220\rangle^*$ systematic row excited. (d) A close to $\langle 110\rangle$ zone axis orientation EDP obtained by tilting only a few degrees away from the exact $\langle 110\rangle$ zone axis orientation. Note the presence of strong blobs of diffuse intensity ("satellite reflections") at the $\mathbf{G}\pm\sim\langle 001\rangle^*$ positions of reciprocal space along with the presence of diffuse streaking running through and connecting these diffuse blobs of intensity along the $\langle 100\rangle^*$ and $\langle 010\rangle^*$ directions of reciprocal space.

intensity along the $\langle 010\rangle^*$ and $\langle 001\rangle^*$ directions of reciprocal space.

These observations are consistent with observations at other zone axis orientations. Fig. 3a, for example, shows an $\sim\langle 551\rangle$ zone axis EDP obtained by tilting $\sim 9^\circ$ away from the exact $\langle 110\rangle$ zone axis orientation keeping a $\langle 2\bar{2}0\rangle^*$ systematic row excited. Note again the strong blobs of diffuse intensity at the $\mathbf{G}\pm\sim\langle 001\rangle^*$ positions of reciprocal space along with the more extended diffuse streaking running through these diffuse blobs along the $\sim\langle 1,1,10\rangle^*$ direction. Fig. 3c, likewise, shows the $\langle 118\rangle$ zone axis EDP obtained by tilting $\sim 10^\circ$ away from the $\langle 001\rangle$ orientation again keeping a $\langle 2\bar{2}0\rangle^*$ systematic row excited. Note again the existence of strong blobs of diffuse intensity at the *Fd*3*m* forbidden $\mathbf{G}\pm\langle 001\rangle^*$ positions of reciprocal space (such as, for example, $\langle 44\bar{1}\rangle^*$ in Fig. 3c) along with the presence of associated diffuse streaking in 'lines' of extended but not unlimited extent running through these blobs along the $\langle 80\bar{1}\rangle^*$ and $\langle 08\bar{1}\rangle^*$ directions respectively.

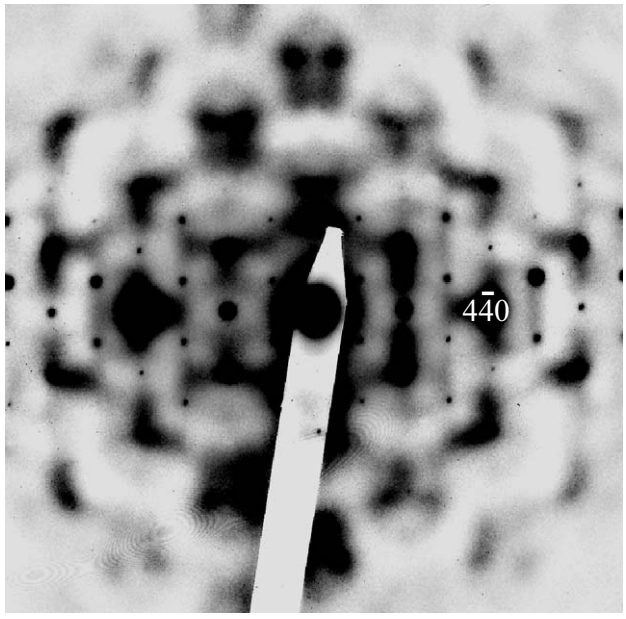

Fig. 4. Typical $\sim\langle 551\rangle$ zone axis EDP of sample 2 for comparison with Fig. 3a.

The polarized character of this diffuse streaking, represented by the fact that the intensity of the $\langle 801\rangle^*$ diffuse streaking is strongest along the $\langle 801\rangle^*$ direction of reciprocal space itself but virtually absent along the orthogonal direction, implies a dominant displacive contribution to the observed intensity distribution while the asymmetry of the diffuse streaking from one side of the $\mathbf{G}\pm\langle 001\rangle^*$ blobs to the other requires a substantial 'size effect' contribution [19]. This 'size effect' contribution is also strongly apparent in the asymmetry of the diffuse distribution surrounding Bragg reflections such as $\langle 044\rangle^*$ in the close to $\langle 001\rangle$ zone axis EDP of Fig. 3b.

Such general behavior was found to be characteristic of $\langle 11w\rangle$ zone axis orientations. On tilting progressively further and further away from the $\langle 001\rangle$ orientation, however, the extent of the diffuse streaking along the $\langle w01\rangle^*$ and $\langle 0w1\rangle^*$ directions of reciprocal space becomes more limited suggesting that the diffuse streaking occurs in one-dimensional lines running simultaneously along all three $\langle 001\rangle^*$ directions of reciprocal space. The fact that these diffuse streaks only run through the $\mathbf{G}\pm\langle 001\rangle^*$ type positions of reciprocal space and not through the *Fd*3*m* allowed Bragg reflections shows that each of the diffuse streaks must have a rational modulation wave-vector component $\mathbf{a}^*$, $\mathbf{b}^*$ or $\mathbf{c}^*$. The reciprocal space positioning of the observed diffuse distribution thus appears to be given by $\mathbf{G}\pm[10l]^*$, $\mathbf{G}\pm[h10]^*$ and $\mathbf{G}\pm[0k1]^*$ respectively. The strong diffuse blobs at the $\mathbf{G}\pm\langle 001\rangle^*$ positions of reciprocal space (such as $\langle 441\rangle^*$ in Fig. 3c) then arise whenever two such diffuse streaks intersect.

5. Preliminary interpretation

Having established that the observed diffuse distribution takes the form $\mathbf{G}\pm[10l]^*$, $\mathbf{G}\pm[h10]^*$ and $\mathbf{G}\pm[0k1]^*$ respectively, the question becomes what is the origin of this structured diffuse scattering and what can we learn from it? Many years ago de Ridder et al. [20], in the context of disordered binary FCC alloys, showed that the same diffuse distribution would arise if the composition of all nearest neighbor tetrahedral clusters in the average FCC array had, as far as possible, the macroscopic composition (see Fig. 3d of [20]).

In the current rather more complicated context, the analogous requirement is not so immediately apparent—which tetrahedral cluster/s should we take, the $O'A_4$ tetrahedra, the $\square B_4$ tetrahedra or the OA_2B_2 tetrahedra or …? As seen above, there are good crystal chemical reasons for assuming that the stoichiometry of each A_4 and B_4 tetrahedra should, as far as possible, take the macroscopic stoichiometry i.e., Bi_3Zn and Nb_3Zn, respectively. Note that such an assumption has immediate consequences for the stoichiometry of the remaining OA_2B_2 tetrahedra i.e., the A_2 stoichiometry can only be Bi_2 or BiZn while the B_2 stoichiometry can only be Nb_2 or NbZn.

Such constraints, while undoubtedly quite restrictive, cannot be expected to, and do not, generate the observed diffuse distribution on their own (see Fig. 5a and below). One reason is that the metal–metal separation vectors within the A_4 and B_4 tetrahedra are all of the form $\frac{1}{4}\langle 110\rangle$ and hence do not correspond to average structure Bravias lattice vectors. In the case of the disordered binary FCC alloys [20], the equivalent metal–metal separation distances were all of the form $\frac{1}{2}\langle 110\rangle$ and hence do correspond to average structure Bravias lattice vectors. This suggests that an additional longer-range constraint on the stoichiometry of metal ion sites separated by $\frac{1}{2}\langle 110\rangle$ is going to be necessary. This was the starting point for the following Monte Carlo study of metal ion ordering and associated structural relaxation.

6. Monte Carlo simulation results

Monte Carlo (MC) simulation with subsequent calculation of model diffraction patterns has become well established as a viable means of interpreting and analyzing diffuse scattering from disordered structures [21–25]. A model of the structure is set up in the computer based on the observed average structure. Interactions between different atomic sites are represented by Hooke's law springs where the length, d_0, of different springs and their corresponding spring constants, k_0, are quantities that may be adjusted to obtain a fit to the observed diffraction data. When there is disorder on particular atomic sites the values of d_0 and k_0 will in general differ for different combinations of atomic species forming each inter-atomic vector.

Given the much stronger scattering power of the A ions relative to the B ions for electron diffraction in conjunction with the results of the above average structure refinement, in particular the order of magnitude larger displacement parameters refined for the A and O′ ions, it is clear that the experimentally observed diffuse distribution will be dominated by the composition induced displacive shifts of the Bi and Zn ions on the pyrochore A sites of the $O'A_2$ sub-structure. We therefore concentrate entirely on the $O'A_2$ corner-connected tetrahedral sub-structure of anti-cristobalite structure type for the purposes of modelling the observed electron diffraction data.

The aim was to investigate the possible ordering of the Bi and Zn ions on the A site and the subsequent structural relaxation. A model crystal was set-up comprising $32\times32\times32$ unit cells each of which contained 16 A cation sites and 8 O′ sites (i.e., 786,432 atomic sites in total). The MC simulation was carried out using only the A cation sites. For calculation of diffraction patterns the O′ atoms were subsequently inserted within each A_4 tetrahedron (see later).

6.1. Ordering of Bi and Zn

Random variables x_{ijkl} were used to represent the occupancy of each A cation site in the model lattice. The indices i, j, k refer to a particular unit cell and l to the site within the cell. A value of $x_{ijkl}=0$ corresponds to that site being occupied by a Zn and $x_{ijkl}=1$ to a Bi. Initially all of the x_{ijkl} were chosen randomly to be 1 with a probability of 0.75 and 0 with a probability of 0.25. In all subsequent simulations these concentrations were maintained since at each step in the MC iteration the variables from two randomly chosen A sites were interchanged. In order to try to order the Bi and Zn cations on the A sites a MC energy of the form

$$E_1=\sum_{\text{all tetrahedra}}(N_{\text{Bi}}-3)^2 \qquad (1)$$

was used. Here N_{Bi} is the number of A sites within a given tetrahedron that are occupied by Bi. The MC iteration was then carried out as follows. Two different A sites i,j,k,l were chosen at random and the energy E_1 was calculated by summing over those tetrahedra which contained the targeted A sites. After interchanging the two selected sites the energy was recalculated and the difference, $\Delta E=E_{\text{new}}-E_{\text{old}}$, obtained. If $\Delta E<0$ then the new configuration was accepted, while for $\Delta E>0$ the new configuration was accepted with probability $P=\exp(-\Delta E/kT)$, but otherwise the system was returned to its original configuration. Iteration was carried out for 200 cycles where a cycle consists of that number of

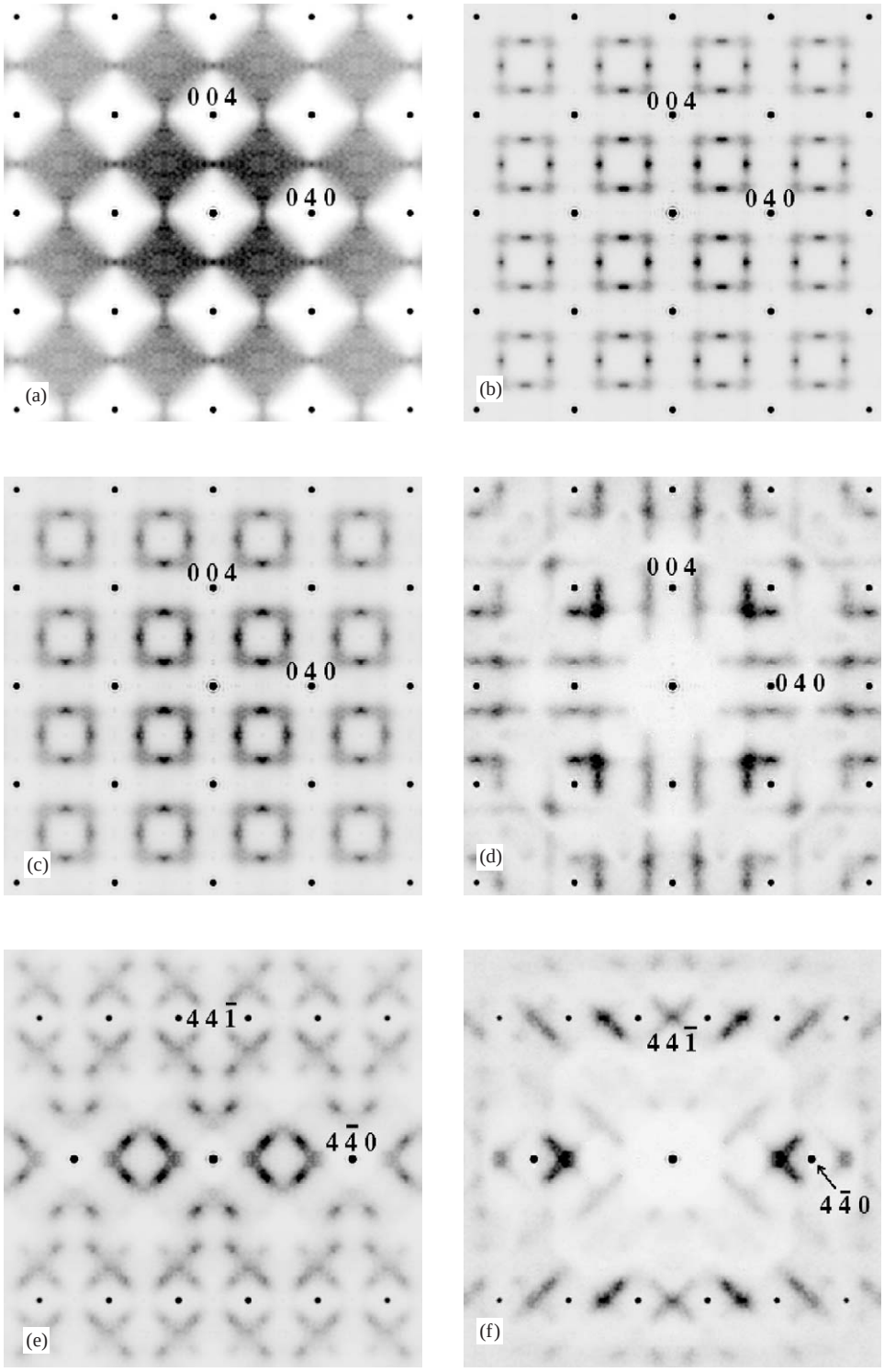

Fig. 5. Diffraction patterns calculated from the MC simulations described in the text. (a)–(d) Correspond to the [001] zone axis orientation. (e) and (f) to the [118] zone axis orientation. (a) Cations ordered using E_1 only. (b) Cations ordered using $\frac{1}{2}E_1 + \frac{1}{2}E_2$. (c)–(f) Cations ordered using $\frac{2}{3}E_1 + \frac{1}{3}E_2$. (d) and (f) same cation ordering as (c) and (e) but with subsequent relaxation using E_3. Calculations were performed using the program DIFFUSE [20].

individual MC steps required to visit each site once on average. A temperature $kT = 0.125$ was used throughout all simulations reported here. This value was chosen after some initial trials to assess the efficiency with which completeness of ordering could be achieved within the 200 cycle simulation. Table 5 gives the fraction of individual tetrahedra containing 0, 1, 2, 3 or 4 Bi ions in the initial distribution and after ordering with energy E_1.

Table 5
Fraction of tetrahedra containing n Bi ions for the various MC models described in the text

Number of Bi ions, n	Fraction of tetrahedra containing n Bi				
	0	1	2	3	4
Random	0.004	0.050	0.211	0.424	0.312
E_1 ordering	0.0	0.0	0.016	0.967	0.017
$\frac{1}{2}E_1+\frac{1}{2}E_2$ ordering	0.0	0.0	0.042	0.916	0.042
$\frac{2}{3}E_1+\frac{1}{3}E_2$ ordering	0.0	0.0	0.024	0.952	0.024

In Fig. 5a we show an example diffraction pattern calculated from this ordered distribution. For each of the tetrahedra an oxygen atom was inserted near the center with a position that was calculated as the weighted mean of the 4 surrounding cations. In this calculation a 'weight' of 0.47 was used for a Bi and 0.53 for a Zn so that in a tetrahedron with 3 Bi and 1 Zn the O′ ion would be shifted towards the Zn. This particular weighting scheme was chosen as to satisfy as nearly as possible the bond valence sum requirements discussed earlier.

It is clear from Fig. 5a that although local ordering of the Bi/Zn ions within the tetrahedra produces structured diffuse scattering this is insufficient in and of itself to produce the sort of longer-range ordering observed in the electron diffraction patterns (cf. with Figs. 3 and 4). To achieve this a longer-range interaction acting within each of the four different sublattices of the FCC anti-cristobalite structure is required. Consequently a second energy term was added to the MC energy. This was of the form

$$E_2 = \sum_{\text{all } 1/2\langle 110\rangle \text{ neighbors}} \delta_{m,n}. \tag{2}$$

Here $\delta_{m,n}$ is unity if both the target and the neighboring sites are occupied by Zn and is zero otherwise. This term, therefore, has the effect of ensuring that there are very few Zn ions in close proximity to any other particular Zn ion.

Two simulations were carried out using E_2 in addition to E_1. In the first case the total MC energy used was $\frac{1}{2}E_1+\frac{1}{2}E_2$, while in the second the energy was $\frac{2}{3}E_1+\frac{1}{3}E_2$. The effect on the [100] diffraction pattern of adding this second energy term is shown in Fig. 5b and c. In Fig. 5b, which corresponds to the $\frac{1}{2}E_1+\frac{1}{2}E_2$ case, it is seen that there is a *motif* of 8 diffuse diffraction spots forming a square centered around the $\langle 022\rangle^*$, $\langle 062\rangle^*$, $\langle 026\rangle^*$ positions. In Fig. 5c, which corresponds to the $\frac{2}{3}E_1+\frac{1}{3}E_2$ case, this *motif* is more blurred with the peaks at the corners of the square having been absorbed into a more continuous streak. Fig. 5e shows the [118] zone axis diffraction pattern obtained from the same simulations as Fig. 5c.

6.2. Relaxation of Bi and Zn positions

Figs. 5a–e were all obtained from simulations in which ordering of cations had been carried out but with no local relaxation of the cation positions i.e., all cations were on their perfect anti-cristobalite lattice sites. In order to assess the effects of local relaxation a further stage of MC simulation was carried out in which neighboring cation–cation distances (forming the edges of the tetrahedra) were subject to a MC energy of the form,

$$E_3 = \sum_{n.n.\text{ cation vectors}} (d - d_0(1+\varepsilon_{m,n}))^2. \tag{3}$$

Here d is the instantaneous length of a given cation–cation distance, d_0, the average cation–cation distance and $\varepsilon_{m,n}$ is a 'size-effect' parameter. For the simulations described here $\varepsilon_{m,n}$ was taken as $+0.06$ for Bi–Bi vectors, -0.06 for Bi–Zn vectors and 0.0 for Zn–Zn vectors (of which there were very few). The value of ± 0.06 corresponds approximately to the magnitude of the distortion required to satisfy the bond-valence sums for Bi and Zn (see earlier).

With the occupancy distribution kept fixed, 200 MC cycles of iteration were performed using the energy E_3 to allow the positions of the cations to relax. This was carried out as follows. A cation site was selected at random and the energy E_3 computed by summing over all cation–cation vectors involving that site. The position of the site was then subjected to a small random shift and the energy computed again. If the new energy was lower then the shifted position was accepted, otherwise the previous position was resumed (this essentially corresponds to performing the relaxation at $kT = 0$). 200 cycles of iteration were found sufficient to achieve a configuration that was considered close to fully relaxed. Diffraction patterns were then computed for comparison with the unrelaxed patterns described above. As before the O atoms were inserted within each tetrahedron using the weighted mean of the four surrounding cation positions. Figs. 5d and f show diffraction patterns of the relaxed distributions for [100] and [118] zone axis orientations, respectively. Comparison with Figs. 5c and 5e shows how the distortion has had a marked effect on the distribution of intensity in the patterns.

Fig. 6 shows (a) $\langle 551\rangle$, (b) [100], (c) [118] and (d) [110] zone axis diffraction patterns simulated using the same relaxed distribution for direct comparison with the equivalent EDPs shown in Fig. 3. While the agreement is by no means perfect, there is clearly rather good qualitative agreement. We therefore believe that the relaxed distribution generated via the above Monte Carlo simulation is providing a good representation of the local short range order and associated structural relaxation in the O′A_2 sub-structure.

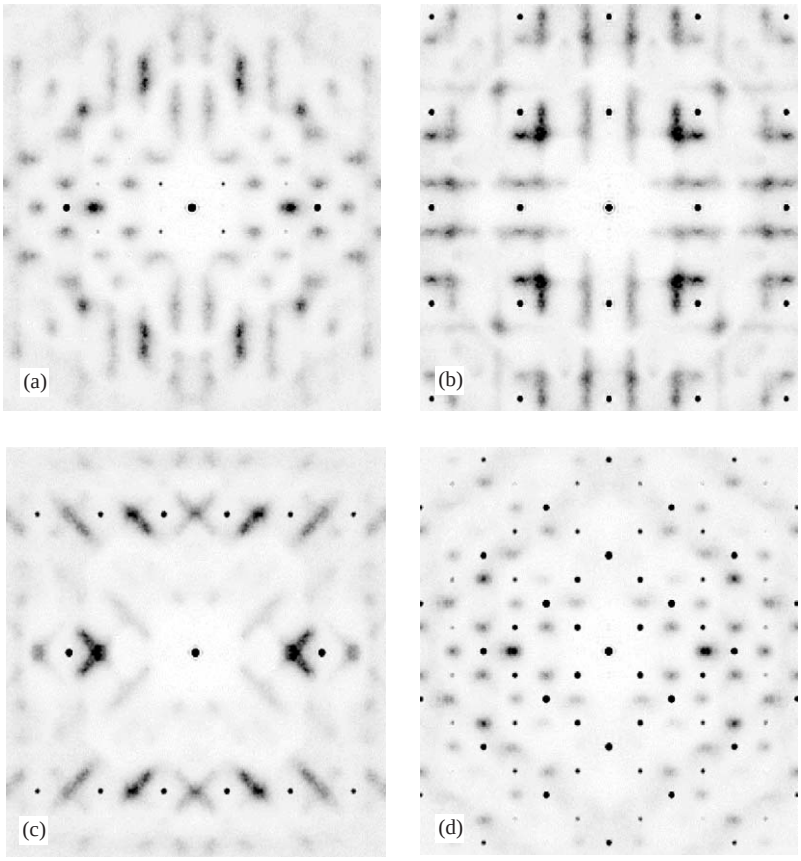

Fig. 6. (a) $\langle 551 \rangle$, (b) [100], (c) [118] and (d) [110] zone axis diffraction patterns simulated using the relaxed $\frac{2}{3}E_1 + \frac{1}{3}E_2$ distribution for direct comparison with the equivalent EDPs shown in Fig. 3. For indexation see Fig. 3.

In addition to observing the changes in the diffraction patterns it is also interesting to show plots of the distribution of atomic positions in unit cells of the fully relaxed simulation. In Fig. 7a we plot the positions of the Bi, Zn and O′ ions from all of the unit cells in the simulation superposed onto a single unit cell. The distribution is shown in projection down [110] since this most clearly shows some interesting features that occur. First, the cations on the *A* sites show very strong anisotropic displacements in the form of a flat disc perpendicular to the local O′–*A*–O′ direction. This is in very good agreement with the anisotropic average structure refinement described earlier and in [10]. A second feature is that the displacements in the plane of the disc are substantially greater for the Bi ions (dark gray) than for the Zn ions (light gray). In light of this result, the average structure data was re-considered. It was found to be possible to fit a model with Zn at $\frac{1}{2},\frac{1}{2},\frac{1}{2}$ and Bi displaced perpendicular to the local O′–*A*–O′ direction as described above with essentially equivalent refinement statistics as Model 3 in Table 1. The data, however, would not support independent refinement of their thermal parameters. Finally it is seen that the method of placing the O′ atoms (black) within each tetrahedron using the weighted mean described above has resulted in a tetrahedral distribution for that site which has a triangular appearance in projection. In Fig. 7b we show a drawing of the structure for comparison.

Finally Fig. 8 shows a one unit cell thick slice of a representative portion of the non-relaxed cation distribution projected along the $\langle 001 \rangle$ direction. The larger black circles correspond to the Zn ions, the larger gray circles to the Bi ions and the small open circles to O′ ions in $O'Bi_3Zn$ tetrahedra. Small dark circles correspond to the small number of O′ ions in $O'Bi_2Zn_2$ tetrahedra or $O'Bi_4Zn_0$ tetrahedra (see Table 5). Note that the unit cell origin has been shifted to an O′ ion so that the four FCC translation related $O'Bi_3Zn$ tetrahedra are contained within one projected unit cell. The negative correlation along neighboring $\frac{1}{2}\langle 110 \rangle$ directions is represented by the fact that the position of the unique Zn ion in each of these 4 neighboring $O'Bi_3Zn$ tetrahedra is almost never the same. This local destruction of the face-centering translations of the $Fd\bar{3}m$ average structure could be thought of as giving rise to the $\mathbf{G} \pm \sim \langle 001 \rangle^*$ "satellite reflections" observed experimentally.

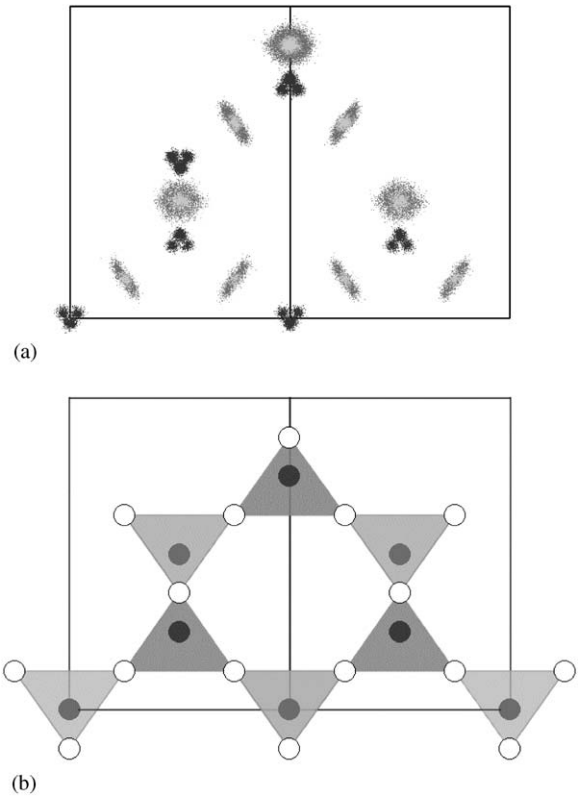

Fig. 7. (a) Plot showing the distribution of atomic sites in the MC simulation corresponding to the diffraction patterns Figs. 5d and f, projected along the ⟨110⟩ direction. All displacements away from the ideal anti-cristobalite atomic sites resulted entirely from the 'size-effect' relaxation using E_3 in Eq. (3). The light gray distribution is that of the Zn^{2+} ions, the dark gray that of the Bi^{3+} ions and the black that of the O′ ions. (b) Corresponding ⟨110⟩ projection of the ideal $O'A_2$ sub-structure. Note that the Bi ions move perpendicular to the local O′–*A*–O′ direction. This is in very good agreement with the anisotropic average structure refinement.

7. Conclusions

Clear evidence in the form of structured diffuse scattering has been found for short range ordering of metal ions and associated strain induced structural relaxation in cubic BZN pyrochlores. The experimentally observed diffuse distribution is dominated by the composition induced displacive shifts of Bi and Zn ions on the pyrochore *A* sites of the $O'A_2$ sub-structure. The compositional and consequent displacive disorder on this $O'A_2$ sub-structure has been qualitatively interpreted via Monte Carlo modelling guided by the insights provided by a bond valence sum analysis of the average crystal structure. Remaining challenges are to integrate the Monte Carlo simulated disorder on this $O'A_2$ sub-structure with the smaller but also crystal chemically important disorder to be expected on the B_2O_6 sub-structure as well as to understand the extent and role of ZnO deficiency in these materials. This, however, is beyond the scope of the current contribution.

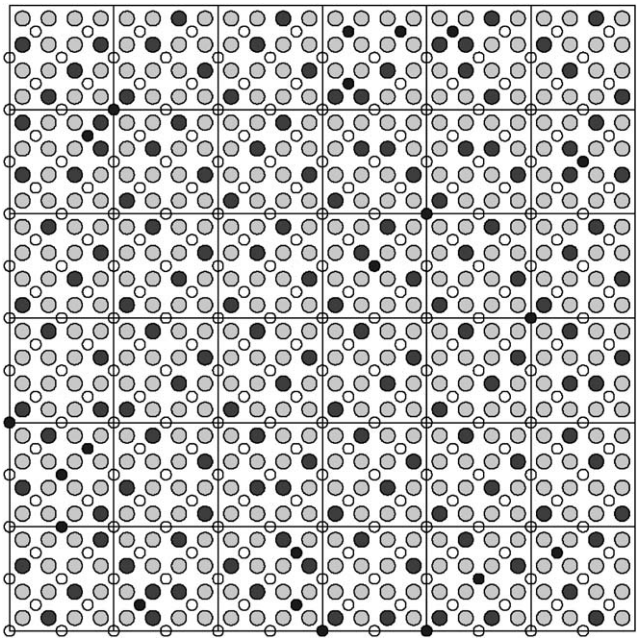

Fig. 8. One unit cell thick slice of a representative portion of the final non-relaxed cation distribution projected along the ⟨001⟩ direction. The larger black circles correspond to Zn ions, the larger gray circles to Bi ions and the small open circles to O′ ions in majority $O'Bi_3Zn$ tetrahedra. Small dark circles correspond to the relatively small number of O′ ions in $O'Bi_2Zn_2$ tetrahedra or $O'Bi_4Zn_0$ tetrahedra (see Table 5). The unit cell origin has been shifted to an O′ ion so that the four FCC translation related $O'Bi_3Zn$ tetrahedra are contained within a projected unit cell.

Acknowledgments

Three of the authors (RLW, TRW and YL) acknowledge the Australian Research Council (ARC) for financial support in the form of an ARC Discovery Grant. A-KL and LN gratefully acknowledge the financial support given by "Veteskapsrådet" (VR) in Sweden. Dr. H.L. Du and Prof. X. Yao of Xi'an Jiaotong University, China are acknowledged for the provision of Sample 1 and for useful discussions.

References

[1] D. Liu, Y. Liu, S.-Q. Huang, X. Yao, J. Am. Ceram. Soc. 76 (1993) 2129.
[2] D.P. Cann, C.A. Randall, T.R. Shrout, Solid State Commun. 100 (1996) 529.
[3] X. Wang, H. Wang, X. Yao, J. Am. Ceram. Soc. 80 (1997) 2745.
[4] M. Valant, P.K. Davies, J. Am. Ceram. Soc. 83 (2000) 147.
[5] W. Ren, S. Trolier-McKinstry, C.A. Randall, T.R. Shrout, J. Appl. Physics 89 (2001) 767.
[6] J.C. Nino, M.T. Lanagan, C.A. Randall, J. Appl. Phys. 89 (2001) 4512.
[7] J.C. Nino, M.T. Lanagan, C.A. Randall, J. Mater. Res. 16 (2001) 1460.

[8] S. Kamba, V. Porokhonskyy, A. Pashkin, V. Bovtun, J. Petzelt, J.C. Nino, S. Trolier-McKinstry, M.T. Lanagan, C.A. Randall, Phys. Rev. B 66 (2002) 054106-1.
[9] I. Levin, T.G. Amos, J.C. Nino, T.A. Vanderah, I.M. Reaney, C.A. Randall, M.T. Lanagan, J. Mater. Res. 17 (2002) 1406.
[10] I. Levin, T.G. Amos, J.C. Nino, T.A. Vanderah, C.A. Randall, M.T. Lanagan, J. Solid State Chem. 168 (2002) 69.
[11] R.D. Shannon, Acta Crystallogr. A 32 (1976) 751.
[12] M.A. Subramanian, G. Aravamudan, G.V. Subba Rao, Prog. Solid State Chem. 15 (1983) 55.
[13] N.E. Brese, M. O'Keeffe, Acta Crystallogr. B 47 (1991) 192.
[14] M. Love, V.D. Scott, Scanning 4 (1981) 11–130.
[15] Technical data found at: http://www.nfl.uu.se
[16] R.L. Withers, J.G. Thompson, Y. Xiao, R.J. Kirkpatrick, Phys. Chem. Miner. 21 (1994) 421.
[17] R.L. Withers, L.C. Otero-Diaz, J.G. Thompson, J. Solid State Chem. 111 (1994) 283.
[18] R.L. Withers, J.G. Thompson, in: P.L. Gai (Ed.), In Situ Microscopy in Materials Research, Kluwer, Boston, 1997, pp. 301–330 (Chapter 13).
[19] B.D. Butler, R.L. Withers, T.R. Welberry, Acta Crystallogr. A 48 (1992) 737.
[20] R. de Ridder, G. van Tendeloo, S. Amelinckx, Acta Crystallogr. A 32 (1976) 216.
[21] T.R. Welberry, B.D. Butler, J. Appl. Crystallogr. 27 (1994) 205.
[22] T.R. Welberry, A.G. Christym, Phys. Chem. Miner. 24 (1997) 24.
[23] T.R. Welberry, S.C. Mayo, J. Appl. Crystallogr. 29 (1996) 353.
[24] B.D. Butler, T.R. Welberry, J. Appl. Crystallogr. 25 (1992) 391.
[25] T.R. Welberry, Th. Proffen, M. Bown, Acta Crystallogr. A 54 (1998) 661.